

Flavours of the Eady Problem

Investigating modal stability and transient energy growth within flat and sloping bottom formulations of the Eady model for baroclinic instability.

Ruth Moorman

Report Submitted November 9, 2018

Assignment 3 for EMSC4050 *Instabilities in Fluids* (with Navid C. Constantinou)

Research School of Earth Sciences, Australian National University

u5808670@anu.edu.au

1. Introduction to baroclinic instability and the standard Eady problem

Baroclinic instability refers to vertical shear instabilities in geophysical fluid flows and occurs in stably stratified, rotating fluids, where isopycnals and isobars are misaligned. In the Earth's atmosphere, this misalignment is generally sustained through the interaction of meridional temperature gradients and planetary rotation. The mechanism by which baroclinicity can lead to instability in a stably stratified fluid can be understood in the context of Figure 1. In Figure 1, solid lines at angle ϕ to the ground represent isopycnals, whilst the dashed lines at angle α to the ground present two possible isobars along which fluid parcels may move whilst conserving mechanical energy. Should an isobar connect fluid parcels A and B, indicating a situation of *positive baroclinicity* ($\nabla p \times \nabla \rho$ points in the positive x direction, which holds when $\phi > \alpha$), interchanging these fluid parcels would lead to a release of potential energy as kinetic energy, amplifying the perturbation. By contrast, should A and C lie on an isobar, we have *negative baroclinicity* ($\nabla p \times \nabla \rho$ points in the negative x direction when $\phi < \alpha$) and interchanging these parcels would lead to an accumulation, as opposed to a release, of potential energy, making the setup statically stable.

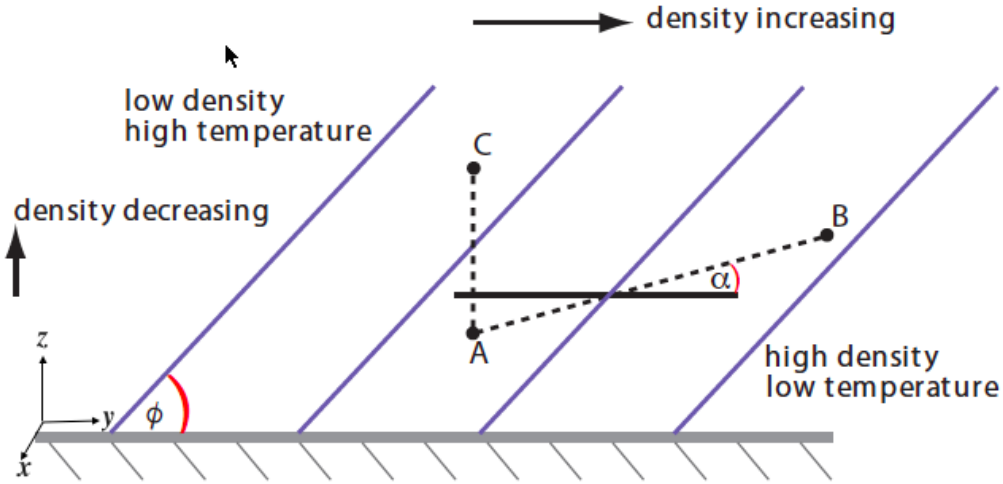


Figure 1: A baroclinic basic state. Figure extracted from Vallis (2017).

Positive baroclinicity occurs in the Earth's oceans and atmosphere. The instabilities that may arise from such baroclinic basic states are most simply understood through the Eady problem.

In the Eady problem, we consider fluid flow under the *quasi-geostrophic approximation*, where vertical velocities (w) are set to zero, whilst horizontal velocities (the zonal, u , and meridional, v , velocities) and buoyancy (b) are described by a pressure dependent stream-function ψ ,

$$u = -\frac{\partial \psi}{\partial y}, \quad v = \frac{\partial \psi}{\partial x}, \quad \text{where} \quad b = -g \frac{\delta \rho}{\bar{\rho}} = f_0 \frac{\partial \psi}{\partial z}, \quad \psi = \frac{p}{\bar{\rho} f_0}. \quad (1)$$

Here we are also invoking the f -plane approximation, wherein the Coriolis frequency is set to a constant f_0 , implying fixed latitude. If we consider a domain of height H , the equations of motion under these approximations are,

$$(\partial_t + u \partial_x + v \partial_y) q = 0, \quad \text{for} \quad 0 < \frac{z}{H} < 1 \quad (\text{in the fluid interior}) \quad (2)$$

$$(\partial_t + u \partial_x + v \partial_y) b = 0, \quad \text{for} \quad z \in \{0, H\} \quad (\text{at the upper and lower boundaries}) \quad (3)$$

where the *quasi-geostrophic potential vorticity* (q) is defined,

$$q = f_0 + \left(\partial_{xx} - \partial_{yy} + \partial_z \frac{f_0}{N^2} \partial_z \right) \psi. \quad (4)$$

The energy of such a flow can be defined,

$$E = \int \frac{1}{2} \left(u^2 + v^2 + \frac{b^2}{N^2} \right) d^3 \mathbf{x} = \int \frac{1}{2} \left[\left(\partial_x \psi \right)^2 + \left(\partial_y \psi \right)^2 + \frac{f_0^2}{N^2} \left(\partial_z \psi \right)^2 \right] d^3 \mathbf{x}. \quad (5)$$

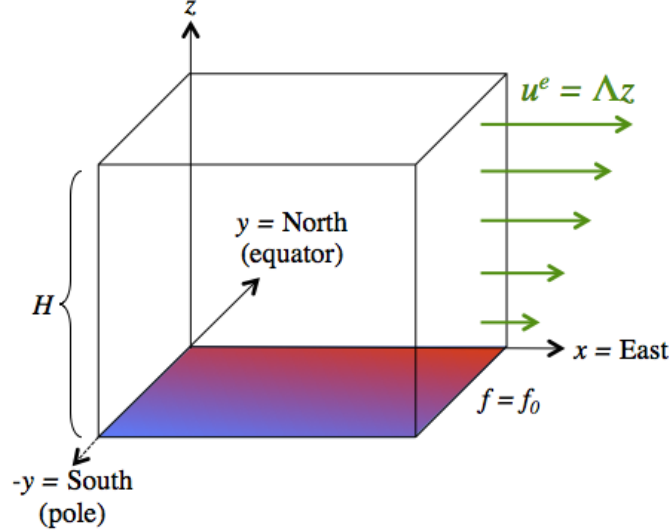


Figure 2: The Eady Problem basic state (oriented for the Southern Hemisphere).

Equations 1-11 are generic to all quasi-geostrophic flows. For the Eady problem, we then consider the basic state in Figure 2 described by,

$$\begin{aligned} N^2(z) &= \text{constant}, & \psi^e &= -\Lambda y z, & u^e &= \Lambda z \\ v^e &= 0, & q^e &= 0, & b^e &= -f_0 \Lambda y, \end{aligned} \quad (6)$$

(where the superscript e indicates the ‘equilibrium’, or basic, state). The domain has rigid, flat upper and lower boundaries. We study the evolution of perturbations independent of y ,

$$\psi = \psi^e + \psi'(x, z, t). \quad (7)$$

Substituting this perturbation into Equations 2 and 3, linearising and converting to non-dimensional quantities gives the following equations of motion,

$$(\partial_{\tilde{t}} + z \partial_{\tilde{x}}) (\partial_{\tilde{x}\tilde{x}} + \partial_{\tilde{z}\tilde{z}}) \tilde{\psi}' = 0, \quad \text{for } 0 < \tilde{z} < 1 \quad (\text{in the fluid interior}) \quad (8)$$

$$\partial_{\tilde{t}} \partial_{\tilde{z}} \tilde{\psi}'_{\tilde{z}=0} - \partial_{\tilde{x}} \tilde{\psi}'_{\tilde{z}=0} = 0, \quad \text{for } \tilde{z} = 0 \quad (\text{at the lower boundary}) \quad (9)$$

$$(\partial_{\tilde{t}} + \partial_{\tilde{x}}) \partial_{\tilde{z}} \tilde{\psi}'_{\tilde{z}=1} - \partial_{\tilde{x}} \tilde{\psi}'_{\tilde{z}=0} = 0, \quad \text{for } \tilde{z} = 1 \quad (\text{at the upper boundary}) \quad (10)$$

and energy equation,

$$E = H^2 \Lambda^2 \int \frac{1}{2} \left[(\partial_{\tilde{x}} \tilde{\psi}')^2 + (\partial_{\tilde{z}} \tilde{\psi}')^2 \right] d\tilde{x} d\tilde{z} \quad (11)$$

where the non-dimensionalised (tilde) quantities are,

$$z = H \tilde{z}, \quad x = \frac{NH}{f_0} \tilde{x}, \quad t = \frac{N}{\Lambda f_0} \tilde{t}, \quad \psi = \frac{NH^2 \Lambda}{f_0} \tilde{\psi}. \quad (12)$$

We then note that the system is homogeneous in \tilde{x} such that $\tilde{\psi}'$ takes a form,

$$\tilde{\psi}'(\tilde{x}, \tilde{z}, \tilde{t}) = \hat{\psi}(\tilde{z}, \tilde{t})e^{i\tilde{k}\tilde{x}} \quad (13)$$

noting $k = \frac{f_0}{NH}\tilde{k}$.

In the standard approach to the Eady problem (see, for example, Vallis 2017), we then assume the following solution form, which simultaneously satisfies Equations 8 - 10,

$$\hat{\psi}(\tilde{z}, \tilde{t}) = A(\tilde{t}) \cosh \tilde{k}\tilde{z} + B(\tilde{t}) \sinh \tilde{k}\tilde{z}. \quad (14)$$

Whilst assuming this solution form is a valid way to analyse the modal stability of the Eady basic state, it is not particularly physically intuitive. In Section 2 of this report I will explore a solution form based on edge-wave interactions that reproduces the modal stability results of the standard approach, yet lends itself more readily to physical interpretation. In Section 3, I will analyse the modal stability of a modified eady model with a sloping lower boundary (replicating the results of Blumsack and Gierasch 1972), and in Section 4, I will extend this analysis to incorporate transient amplifications of perturbations that do not grow exponentially, and so are not covered by modal stability analysis.

2. Edge wave interpretation of the Eady problem

An alternative to assuming a perturbation stream-function that satisfies both upper and lower boundary conditions (Equation 14), is to consider the upper and lower portions of the domain independently before attempting to combine the results. In this way we can envisage the perturbation as two *edge waves* propagating along the upper and lower boundaries of the domain, which are independently stable, yet may combine to generate instabilities.

Equations 8 and 9 (the bulk fluid and lower boundary condition) may be solved by the following perturbation stream-function,

$$\tilde{\psi}'_B = A_B e^{i\tilde{k}(\tilde{x} - \frac{1}{\tilde{k}}\tilde{t})} e^{-\tilde{k}\tilde{z}}, \quad (15)$$

whilst Equations 8 and 10 (the bulk fluid and upper boundary condition) may be solved by,

$$\tilde{\psi}'_T = A_T e^{i\tilde{k}(\tilde{x} - (1 - \frac{1}{\tilde{k}})\tilde{t})} e^{\tilde{k}(\tilde{z} - 1)}. \quad (16)$$

Note the subscripts B and T refer to the bottom and top edge waves. So we have two perturbation stream-functions that *separately* satisfy the top and bottom boundary conditions. Equations 15 and 16 describe two edge-waves, one at the bottom boundary propagating eastward at a speed $c = \frac{1}{\tilde{k}}$, and one at the top boundary propagating eastward at a speed $c = 1 - \frac{1}{\tilde{k}}$. Note that since c is purely real for both edge-waves, these structures are modally stable. The initial perturbation stream-functions and direction of propagation are illustrated in Figure 3.

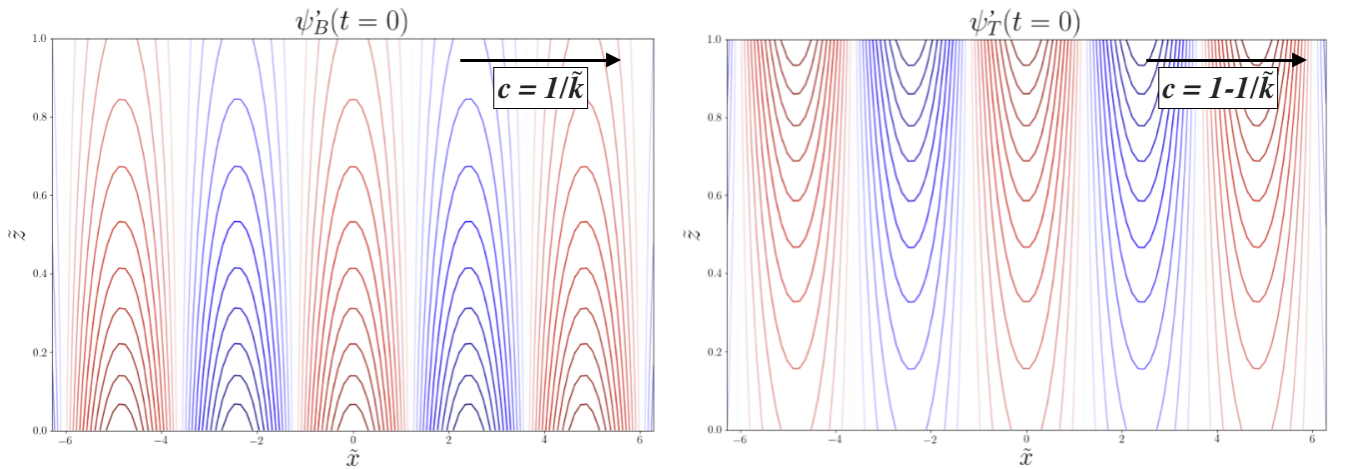
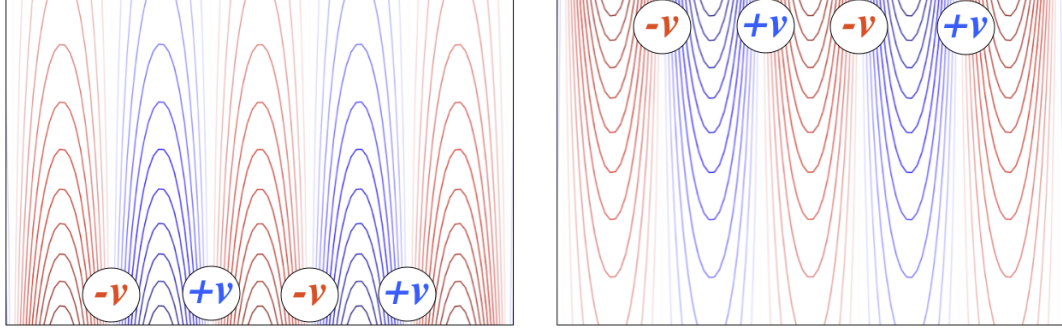
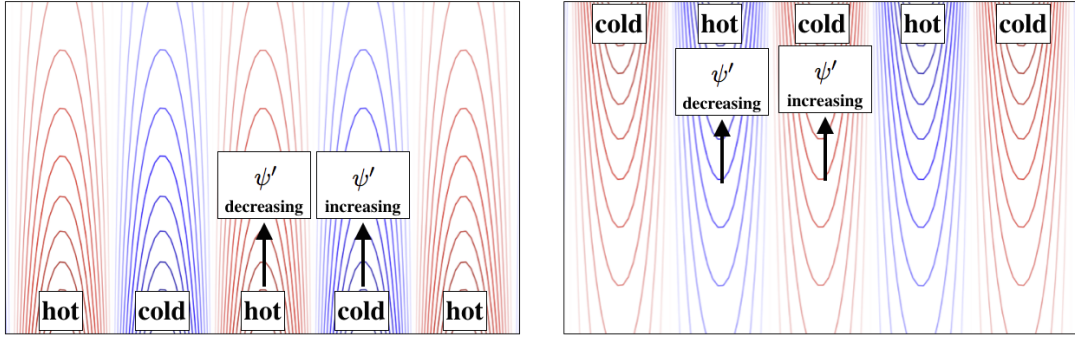


Figure 3: Edge wave solutions for the lower (*left*) and upper (*right*) boundary conditions. A_B , A_T and \tilde{k} have been set to 1. Red and blue contours correspond to positive and negative values of the stream-function respectively.

In order to interpret these edge waves in an atmospheric context, recall that $v = \partial_x \psi'$, $u = -\partial_y \psi' = 0$ (since we are considering an initial perturbation that is a function of only x and z), and $w = 0$ (from the quasi-geostrophic approximation). Secondly, recall the buoyancy expression, $b = f_0 \partial_z \psi'$, noting that regions of positive buoyancy can be interpreted as warm regions, and regions of negative buoyancy can be interpreted as cool regions. Figure 4 demonstrates how this translates to the initial edge waves in Figure 3 in the Southern Hemisphere (where f_0 is negative). Note that the top edge wave propagates to the west, instead of the east, when the background shear flow is neglected.



(a) $v = \partial_x \psi'$. Negative v values bring warm air south from the equator whilst positive v values bring cold air north from the poles (as per Figure 2).



(b) $b = f_0 \partial_z \psi'$. Positive ψ' nodes correspond to warm regions on the lower boundary correspond and cold regions on the upper boundary.

Figure 4: Physical interpretation of edge-wave patterns. Meridional inflows of warm and cold air pictured in (a) would cause the hot and cold nodes in (b) propagate to the east (for the bottom edge-wave) and to the west (for the top edge-wave).

Now that we have this physical picture of each edge-wave, we can establish expectations of how these edge-waves would behave if they were in the same domain. Figure 5 shows two possible ways these top and bottom edge waves could combine. If the bottom edge-wave is phase shifted to the west, as in Figure 5 (a), the bottom edge-wave brings warm (cold) air into the cold (warm) nodes of the top edge-wave, dampening the perturbation. If the bottom edge-wave is shifted to the east as in Figure 5 (b), however, the effect is opposite and meridional flows initiated by the top and bottom edge waves act to amplify the temperature perturbations. If the edge waves were stacked directly on top of one another, with no phase shift, the temperature in the hot and cold nodes would neither increase nor decrease, since $v = 0$ at the centre of each mode. The speed of the edge-waves may increase, however, as the temperature anomaly in the inter-node regions is amplified.

From this simple physical argument, we would expect to find instability when top and bottom edge-waves are offset as in Figure 5 (b) and, critically, travel eastwards at the same speed such that the amplifying geometry is retained through time. This would require $1 - 1/\tilde{k} = 1/\tilde{k}$ i.e. $\tilde{k} = 2$ for sustained perturbation growth. We can now test this intuition by assuming solutions to Equations 8 - 10 that are a linear combination of these top and bottom edge-waves,

$$\hat{\psi}(\tilde{z}, \tilde{t}) = \alpha(\tilde{t})e^{-\tilde{k}\tilde{z}} + \beta(\tilde{t})e^{\tilde{k}(\tilde{z}-1)}. \quad (17)$$

Substituting this solution form into the bottom and top boundary conditions (Equations 9 and 10) provides the following differential equations,

$$-\partial_{\tilde{t}}\alpha + e^{-\tilde{k}}\partial_{\tilde{t}}\beta = i\alpha + ie^{-\tilde{k}} \quad (18)$$

$$-e^{-\tilde{k}}\partial_{\tilde{t}}\alpha + \partial_{\tilde{t}}\beta = i\tilde{k}e^{-\tilde{k}}\alpha - i\tilde{k}\beta + ie^{-\tilde{k}}\alpha + i\beta \quad (19)$$

which can be expressed as the following differential system,

$$\frac{\partial}{\partial \tilde{t}} \begin{pmatrix} \alpha \\ \beta \end{pmatrix} = \underbrace{\begin{pmatrix} -1 & e^{-\tilde{k}} \\ -e^{-\tilde{k}} & 1 \end{pmatrix}^{-1} \begin{pmatrix} i & ie^{-\tilde{k}} \\ ie^{-\tilde{k}}(1+\tilde{k}) & i(1-\tilde{k}) \end{pmatrix}}_{\mathbb{A}} \begin{pmatrix} \alpha \\ \beta \end{pmatrix}. \quad (20)$$

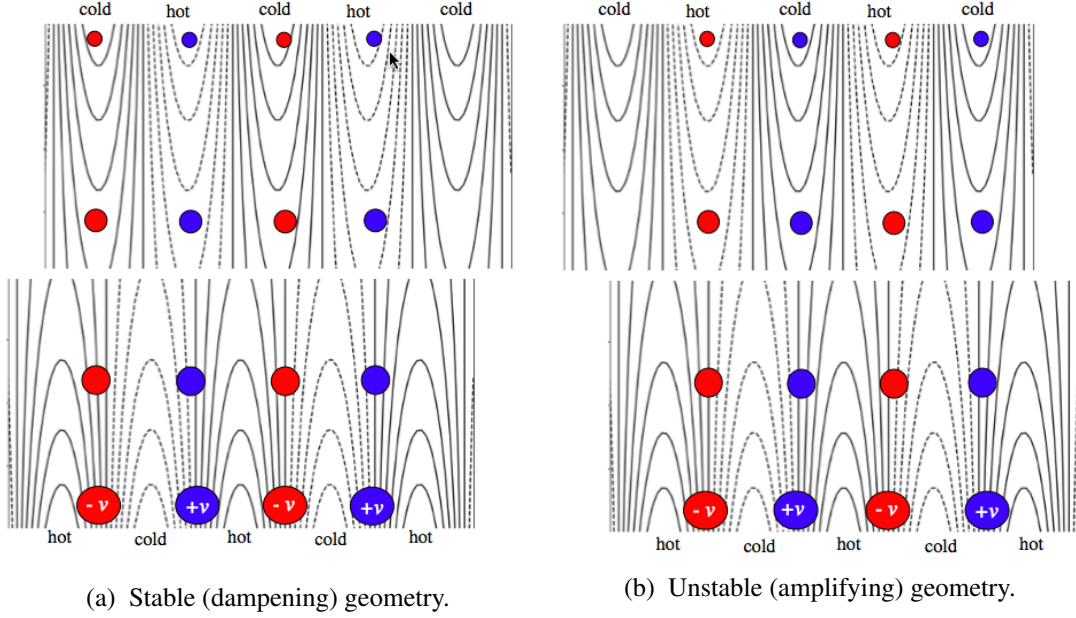


Figure 5: Meridional velocities (v) associated with the bottom boundary edge-wave pull warm or cool air into the plane at the upper boundary, which may counter (a) or amplify (b) the existing temperature anomaly. Velocities associated with the upper edge-wave are not shown but similarly dampen or amplify the lower boundary temperature anomaly in (a) and (b) respectively.

The eigenvalues, σ , of the differential operator \mathbb{A} correspond to the exponential growth rates of the perturbation and so reveal the modal stability of the system. Figure 6 shows how the positive real component of σ varies with \tilde{k} . Note that this plot is identical to that presented by Xihan for the first project, which assumed a solution of the form in Equation 14. Modal instability occurs for a range of \tilde{k} values, not just for $\tilde{k} = 2$ as a straightforward interpretation of the edge-waves described by Equations 15 and 16 might suggest, as the group speeds of each edge-wave are not independent when they share a domain and so are not simply a function of \tilde{k} . There is an upper bound to the values of \tilde{k} capable of generating instability (~ 2.4), since, as \tilde{k} grows, the edge waves become more confined to the upper and lower boundaries until they no longer interact.

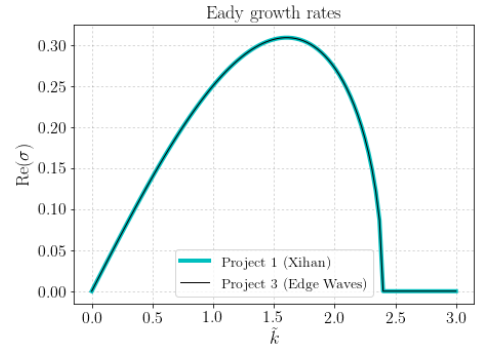


Figure 6: Growth rates (σ) of the system perturbation as a function of \tilde{k} .

Figure 7 presents the perturbation stream-function,

$$\tilde{\psi}'(\tilde{x}, \tilde{z}, \tilde{t}) = \left(\alpha(\tilde{t})e^{-\tilde{k}\tilde{z}} + \beta(\tilde{t})e^{\tilde{k}(\tilde{z}-1)} \right) e^{i\tilde{k}\tilde{x}} \quad (21)$$

where \tilde{k} is set to $\tilde{k}_{\max} (\approx 1.62)$, the value corresponding to the greatest growth rate in Figure 7. Here α and β are set to,

$$\begin{pmatrix} \alpha(\tilde{t}) \\ \beta(\tilde{t}) \end{pmatrix} = e^{\sigma t} \mathbf{v} \quad (22)$$

where σ is the maximum real eigenvalue of \mathbb{A} for $\tilde{k} = \tilde{k}_{\max}$ and \mathbf{v} its corresponding eigenvector. Note when comparing to Figure 5 that the positive (red) contours correspond to warm anomalies in the lower domain but cold anomalies in the upper domain (and vice versa for the negative contours). As anticipated, we see temperature anomalies on the upper and lower boundaries offset as in Figure 5 (b) propagating to the east at the same speed. These perturbations are growing in magnitude, suggesting instability.

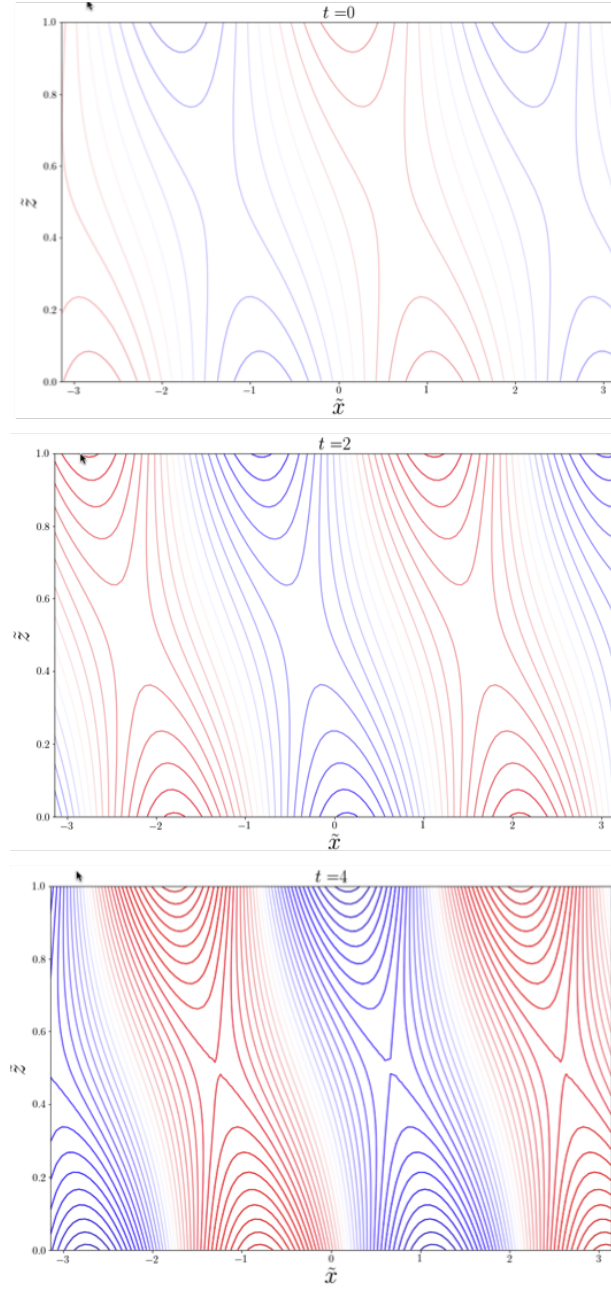


Figure 7: Plot of $\tilde{\psi}'(\tilde{x}, \tilde{z}, \tilde{t})$ for $\tilde{k} = \tilde{k}_{\max} (\approx 1.62)$. Exact magnitudes of $\tilde{\psi}$ are not shown, as they are known only to a scale factor, but contour levels are the same for each plot so we can see that the magnitude of the perturbation stream-function is growing in time. Propagation of the initial wave pattern to the east (positive x) is clearly visible.

3. Modal stability analysis of the sloped bottom Eady problem

Blumsack and Gierasch (1972) extended the Eady problem to incorporate a sloping rigid lower boundary, an adjustment they argued was particularly relevant to Martian topography. They include this sloping bottom boundary by introducing a slope parameter, which I will call μ , which can be interpreted as,

$$\mu = \frac{\text{slope of the ground}}{\text{slope of the isentropes}}. \quad (23)$$

Figure 8 illustrates this parameter, yet is slightly misleading, as it would suggest that that height of the domain H is

impacted by μ for non-zero values of y . In actuality, μ only influences behaviour at the bottom boundary. It is independent of y and effects the system in a purely local sense in that, at every point in the domain, the bottom boundary is angled according to the value of μ but effectively remains at $z = 0$. Thus this formulation neglects the effect of a changing H as the ground slopes towards or away from the upper boundary. Nonetheless it may be interesting to explore, since the height of topography may be assumed negligible compared to the atmospheric height (e.g. height of the troposphere on Earth) in most scenarios. The f -plane approximation already constrains the Eady problem to latitudinally local analysis, so we may assume H would not drastically change over such an interval.

Blumsack and Gierasch (1972) incorporate μ into the Eady equations of motion (Equations 8 - 10) by including it purely in the bottom boundary condition as below,

$$\partial_{\tilde{z}\tilde{t}}\tilde{\psi}'_{\tilde{z}=0} - (1 - \mu)\partial_{\tilde{x}}\tilde{\psi}'_{\tilde{z}=0} = 0, \quad \text{for } \tilde{z} = 0 \quad (\text{at the lower boundary}). \quad (24)$$

As with the flat bottomed Eady problem, we assume a perturbation of the form,

$$\tilde{\psi}'(\tilde{x}, \tilde{z}, \tilde{t}) = \hat{\psi}(\tilde{z}, \tilde{t})e^{ik\tilde{x}} \quad (25)$$

which reduces the Equations 8 - 10 to,

$$(\partial_{\tilde{t}} + ik\tilde{z})(\partial_{\tilde{z}\tilde{z}} - \tilde{k}^2)\hat{\psi} = 0, \quad \text{for } 0 < \tilde{z} < 1 \quad (26)$$

$$\partial_{\tilde{z}\tilde{t}}\hat{\psi}_{\tilde{z}=0} - (1 - \mu)ik\hat{\psi}_{\tilde{z}=0} = 0 \quad \text{for } \tilde{z} = 0 \quad (27)$$

$$(\partial_{\tilde{t}} + ik)\partial_{\tilde{z}}\hat{\psi}_{\tilde{z}=1} - ik\hat{\psi}_{\tilde{z}=1} = 0 \quad \text{for } \tilde{z} = 1 \quad (28)$$

The inclusion of μ changes the differential operator \mathbb{A} (defined such that $d\phi'/dt = \mathbb{A}\phi'$ where ϕ' contains the perturbation fields). Instead of using edge-waves to analytically derive \mathbb{A} as in Section 2, for this problem I elected to discretise the equations of motion and study the system numerically.

For the discretisation we take,

$$\tilde{z} \rightarrow \begin{bmatrix} z_1 = 0 \\ z_2 \\ \vdots \\ z_{n_z-1} \\ z_{n_z} \end{bmatrix}, \quad \hat{\psi}(\tilde{z}, \tilde{t}) \rightarrow \begin{bmatrix} \psi_1 = \hat{\psi}(0, t) \\ \psi_2 \\ \vdots \\ \psi_{n_z-1} \\ \psi_{n_z} = \hat{\psi}(z_{n_z}, t) \end{bmatrix} \quad (29)$$

with δ as $z_i - z_{i-1}$. Applying this discretisation to the Equation 26 gives,

$$\begin{aligned} & \partial_{\tilde{t}} \left(\frac{\psi_{j+1} - 2\psi_j + \psi_{j-1}}{\delta^2} - \tilde{k}^2 \psi_j \right) \\ &= -ik\tilde{z}_j \left(\frac{\psi_{j+1} - 2\psi_j + \psi_{j-1}}{\delta^2} - \tilde{k}^2 \psi_j \right), \quad j \in \{1, 2, \dots, n_z\} \end{aligned} \quad (30)$$

This expression includes two variables ψ_0 and ψ_{n_z+1} which are not assigned values in the discretisation scheme, as such we need to replace them with defined values by analysing the boundary conditions and incorporating the slope, μ , into the discretised system. We look at the equations that apply at $j = 1$. The lower boundary condition equation (Equation 27) requires,

$$\partial_{\tilde{t}} \left(\frac{\psi_2 - \psi_0}{2\delta} \right) = (1 - \mu)ik\psi_1 \quad (31)$$

whilst the bulk fluid equation (Equation 26) evaluated at $j = 1$ requires,

$$\partial_{\tilde{t}} \left(\frac{\psi_2 - 2\psi_1 + \psi_0}{\delta^2} - \tilde{k}^2 \psi_1 \right) = -ik\tilde{z}_1 \left(\frac{\psi_2 - 2\psi_1 + \psi_0}{\delta^2} - \tilde{k}^2 \psi_1 \right) \quad (32)$$

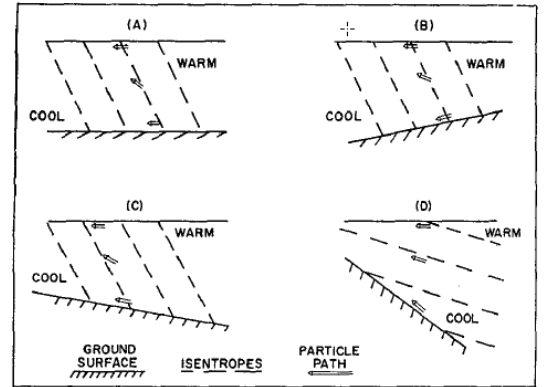


Figure 8: The slope parameter μ (figure extracted from Blumsack and Gierasch 1972).

(A) depicts the classic Eady model, with $\mu = 0$, (B) shows a small negative μ (described as typical of Martian topography), (C) shows a small positive μ , and (D) a large positive μ .

i.e.

$$\partial_{\tilde{t}} \left(\frac{\psi_2 - 2\psi_1 + \psi_0}{\delta^2} - \tilde{k}^2 \psi_1 \right) = 0 \quad (33)$$

since $z_1 = 0$. Taking $2/\delta$ times Equation 31 and adding the result to Equation 33 provides an expression independent of ψ_0 ,

$$\partial_{\tilde{t}} \left(\frac{2\psi_2 - 2\psi_1}{\delta^2} - \tilde{k}^2 \psi_1 \right) = (1 - \mu) \frac{2i\tilde{k}}{\delta} \psi_1. \quad (34)$$

By a similar means we eliminate the extrapolated point from the upper boundary discretisation to extract,

$$\partial_{\tilde{t}} \left(\frac{-2\psi_{n_z} + 2\psi_{n_z-1}}{\delta^2} - \tilde{k}^2 \psi_{n_z} \right) = -i\tilde{k} \left(\frac{-2\psi_{n_z} + 2\psi_{n_z-1}}{\delta^2} - \tilde{k}^2 \psi_{n_z} \right) - \frac{2i\tilde{k}}{\delta} \psi_{n_z}. \quad (35)$$

Combining Equations 30, 34 and 35 allows us to construct the discretised version of the operator \mathbb{A} ,

$$\mathbb{A} = (\partial_{zz} - \tilde{k}^2)^{-1} \left(-i\tilde{k}\mathbb{Z}(\partial_{zz} - \tilde{k}^2) + ik\mathbb{B} \right) \quad (36)$$

such that,

$$\partial_{\tilde{t}} \psi' = \mathbb{A} \psi'. \quad (37)$$

Here,

$$\partial_{zz} - k^2 = \frac{1}{\delta^2} \begin{bmatrix} -2 & -2 & & & \\ 1 & -2 & 1 & & \\ & \ddots & \ddots & \ddots & \\ & & 1 & -2 & 1 \\ & & & 2 & -2 \end{bmatrix} - k^2 \mathbb{I}, \quad (38)$$

$$\mathbb{Z} = \begin{bmatrix} z_1 = 0 & & & & \\ & z_2 & & & \\ & & \ddots & & \\ & & & z_{n_z-1} & \\ & & & & z_{n_z} \end{bmatrix}, \quad (39)$$

and,

$$\mathbb{B} = \begin{bmatrix} \frac{2(1-\mu)}{\delta} & & & & \\ & 0 & & & \\ & & \ddots & & \\ & & & 0 & \\ & & & & -\frac{2}{\delta} \end{bmatrix}. \quad (40)$$

With this discretised version of \mathbb{A} we can analyse the modal stability of the sloped bottom Eady problem. Figure 9 shows the maximum real eigenvalues of \mathbb{A} as a function of \tilde{k} and μ , reproducing analysis from Blumsach and Gierasch's 1972 paper. A transect at $\mu = 0$ replicates Figure 6. As with the flat bottomed case, Figure 9 can be interpreted in the context of edge-wave interactions. The addition of the slope parameter μ alters the bottom edge-wave expression such that it propagates eastward with a speed $c_{\text{bottom}} = \frac{1-\mu}{\tilde{k}}$ as opposed to $\frac{1}{\tilde{k}}$, whilst the top edge-wave is unaffected and retains the speed $c_{\text{top}} = 1 - \frac{1}{\tilde{k}}$. Noting this, we would expect modal instabilities to cluster about the line $\tilde{k} = 2 - \mu$ (which solves $c_{\text{bottom}} = c_{\text{top}}$), and indeed this is observed in Figure 9. This relation does not hold for the entire parameter space, however, with no instabilities indicated for $\mu > 1$ irrespective of the value of \tilde{k} . This is because the top edge wave propagates eastward for the range of \tilde{k} values plotted, and if $\mu > 1$ we have that $c_{\text{bottom}} < 0$ (indicating westward propagation) meaning the edge-waves cannot phase lock in a manner that amplifies perturbations.

Figure 10 shows eigenvectors associated with unstable σ values in the parameter space of Figure 9, these are the initial perturbations that would grow with rate σ . We can see that as \tilde{k} grows, perturbations become more confined to the upper and lower boundaries, with modal instabilities eventually disappearing for large \tilde{k} when edge-waves grow to

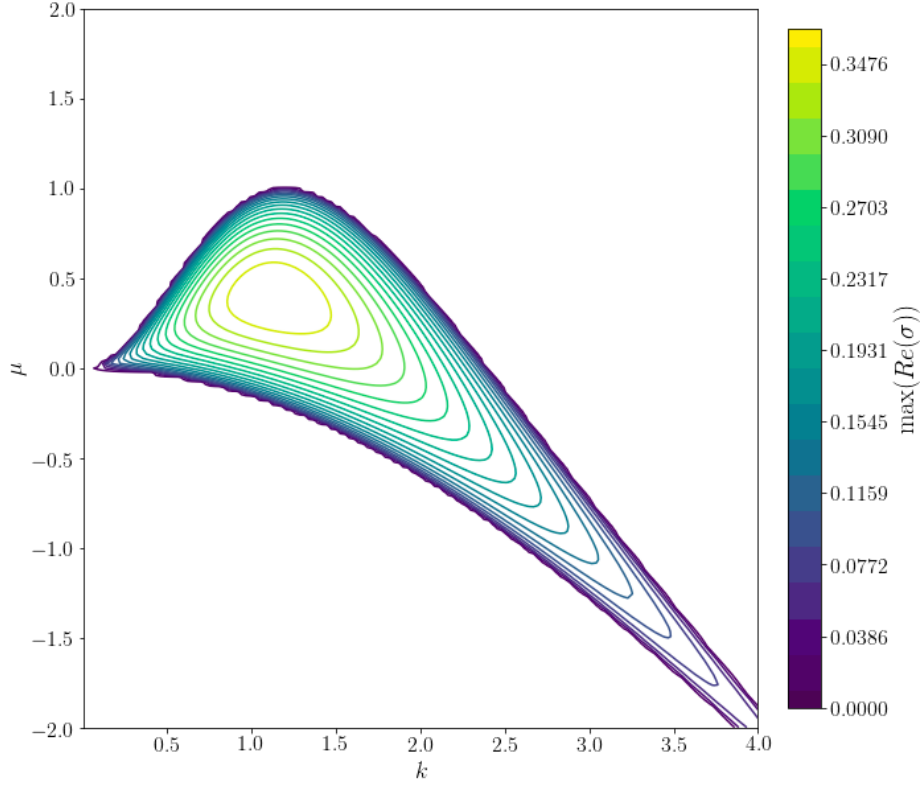


Figure 9: Perturbation growth rate ($\sigma = \max(\text{Re}(\text{eig}(\mathbb{A})))$) as a function of the slope parameter μ and horizontal wavenumber \tilde{k} . Blank regions indicate modally stable parts of the parameter space.

small to interact. It was further found that unstable eigenmodes with positive μ values tended to have more energy in the upper-edge wave whilst eigenmodes with negative μ values had more energy in the lower edge-wave. This analysis simply reproduced the findings of Blumsack and Gierasch (1972), in the next section, I will expand this analysis to incorporate transient energy growth (i.e. general, as opposed to modal, stability analysis).

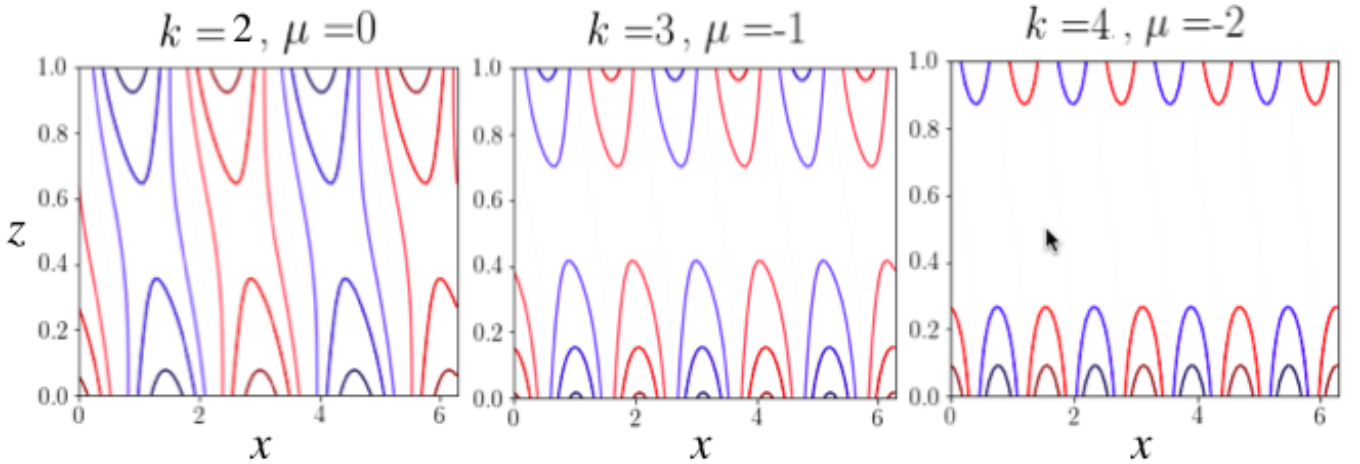


Figure 10: Eigenvectors (i.e. initial perturbation fields) of \mathbb{A} corresponding to modally unstable combinations of \tilde{k} and μ (these in particular follow $\tilde{k} = 2 - \mu$).

4. General stability analysis of the sloped bottom Eady problem

In order to determine whether perturbations can temporarily grow in the sloping bottom Eady model even when the system is modally stable, we will investigate its energy equation (which is identical to the energy equation of the flat bottom Eady problem, Equation 11). Substituting a solution of the form,

$$\tilde{\psi}'(\tilde{x}, \tilde{z}, \tilde{t}) = \hat{\psi}(\tilde{z}, \tilde{t})e^{i\tilde{k}\tilde{x}} \quad (41)$$

into the energy equation takes some care. We note that we only want the real part of the the quadratic in the integral, yet $\hat{\psi}$ could feasibly be complex, so we note

$$\text{Re}(\hat{\psi}e^{ik\tilde{x}}) = \frac{\hat{\psi}e^{ik\tilde{x}} + \hat{\psi}^*e^{-ik\tilde{x}}}{2} \quad (42)$$

where the asterisk connotes the complex conjugate. Then,

$$(\partial_{\tilde{x}}\psi')^2 = \frac{\tilde{k}^2\hat{\psi}^*e^{-2ik\tilde{x}}}{4} - \frac{\tilde{k}^2\hat{\psi}e^{2ik\tilde{x}}}{4} + \frac{\tilde{k}^2\hat{\psi}\hat{\psi}^*}{2} \quad (43)$$

and,

$$(\partial_{\tilde{z}}\psi')^2 = \frac{e^{2ik\tilde{x}}(\partial_{\tilde{z}}\hat{\psi})^2}{4} + \frac{e^{-2ik\tilde{x}}(\partial_{\tilde{z}}\hat{\psi}^*)^2}{4} + \frac{\partial_{\tilde{z}}\hat{\psi}\partial_{\tilde{z}}\hat{\psi}^*}{2}. \quad (44)$$

Further, we can note that,

$$\hat{\psi}\hat{\psi}^* = |\hat{\psi}|^2 \quad \partial_{\tilde{z}}\hat{\psi}\partial_{\tilde{z}}\hat{\psi}^* = |\partial_{\tilde{z}}\hat{\psi}|^2 \quad (45)$$

before substituting these expressions into Equation 11 and evaluating. As we integrate over a wavelength in the x direction, the components of the integral with e^{2ikx} or e^{-2ikx} factors will go to zero. And so we are left with the following energy expression,

$$\frac{E}{2\pi/\tilde{k}} = \frac{H^2\Lambda^2}{4} \int (|\partial_{\tilde{z}}\hat{\psi}|^2 + \tilde{k}^2|\hat{\psi}|^2)d\tilde{z}. \quad (46)$$

Now we want to discretise this integral, from here on I will neglect the scale factor $\frac{\pi H^2\Lambda^2}{\tilde{k}^2}$ for simplicity. Using the trapezoidal rule to approximate the integral and a finite difference discretisation of the differentials we obtain,

$$E \propto [\psi_1^*, \dots, \psi_{n_z}^*] \mathbb{M} \begin{bmatrix} \psi_1 \\ \vdots \\ \psi_{n_z} \end{bmatrix} = (\psi'(t), \mathbb{M}\psi'(t)) \text{ where } \mathbb{M} = \frac{1}{\delta} \begin{bmatrix} 1 + \frac{\delta\tilde{k}^2}{2} & -1 & 0 & \dots & 0 \\ -1 & 2 + \delta\tilde{k}^2 & -1 & \ddots & \vdots \\ 0 & \ddots & \ddots & \ddots & 0 \\ \vdots & \ddots & -1 & 2 + \delta\tilde{k}^2 & -1 \\ 0 & \dots & 0 & -1 & 1 + \frac{\delta\tilde{k}^2}{2} \end{bmatrix}. \quad (47)$$

It was demonstrated in the lectures that if the energy of a system $\partial_t\psi = \mathbb{A}\psi$ is an inner product of the form $(\psi(t), \mathbb{M}\psi(t))$ where \mathbb{M} is a self-adjoint positive definite operator, then the energy growth at time t is bound from above by the maximum real eigenvalue of, and from below by the minimum real eigenvalue of, the following quantity,

$$e^{\mathbb{A}_{\mathbb{M}}^\dagger t} e^{\mathbb{A}_{\mathbb{M}} t}, \quad \text{where } \mathbb{A}_{\mathbb{M}} = \mathbb{M}^{1/2} \mathbb{A} \mathbb{M}^{-1/2}.$$

Note here the superscript \dagger refers to the conjugate transpose. Using this insight, we define the growth at time t of a given perturbation, q to be,

$$g = \frac{E(t)}{E(0)} = \max(\text{Re}(\text{eig}(e^{\mathbb{A}_{\mathbb{M}}^\dagger t} e^{\mathbb{A}_{\mathbb{M}} t}))) \quad (48)$$

and use this to define an *effective growth rate* σ_e that represents the exponential (i.e. modally unstable) growth rate σ that would be required to obtain the energy growth g at time t ,

$$\sigma_e = \frac{\log g}{2t}. \quad (49)$$

We want to know whether sloping bottom Eady systems that are modally stable (i.e. $\sigma = 0$) could have transiently growing perturbations (i.e. $\sigma_e \neq 0$). Figure 11 shows a timeseries of contour plots that are similar to Figure 9 (and cover the same μ, \tilde{k} parameter space) except that the contours represent σ_e values for the given t , as opposed to σ values which are relevant at $t \rightarrow \infty$. We can see that at $t = 1$ there is energy growth for the entire parameter space, and that as t increases, the σ_e contour plots approach the modal stability plot in Figure 9. This too makes sense in the context of the edge wave interaction arguments in Section 2. We only expect energy growth to be exponential, and so persist as $t \rightarrow \infty$, for those regions of the μ, \tilde{k} parameter space where the upper and lower edge-waves can become phase locked, allowing them to propagate whilst retaining an energy amplifying geometry. However, edge-waves that are not phase locked, and so cannot sustain an energy amplifying geometry, can still periodically gain and lose perturbation energy as they move from energy amplifying structures, to energy dampening structures, and back again. Hence we see that perturbations can grow outside the unstable region on Figure 9, but that they stabilise, instead of growing exponentially, when the edge waves of the system cannot propagate at the same speed.

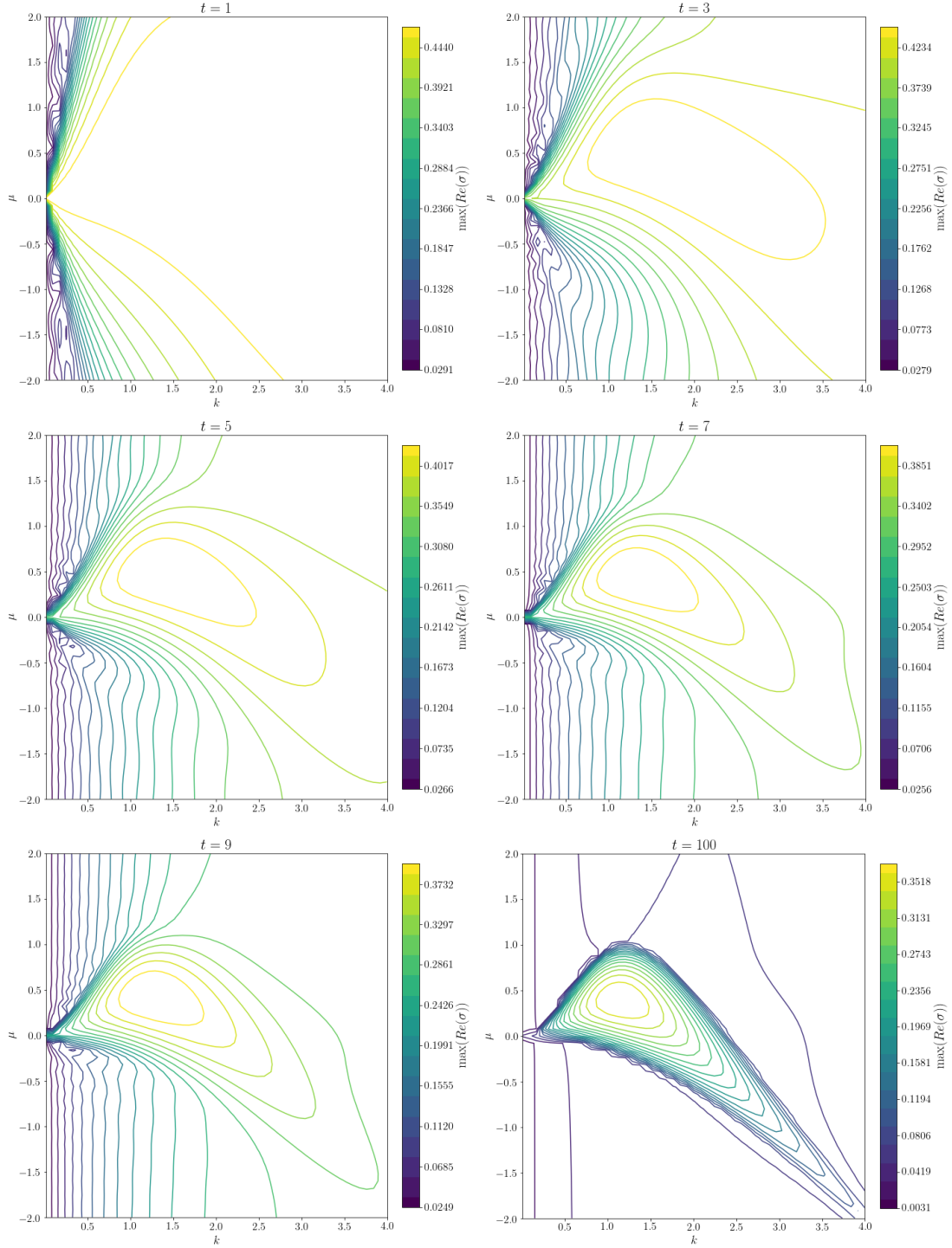


Figure 11: Effective growth rates for the sloping bottom Eady model at $t = 1, 3, 5, 7, 9 \dots 100$ demonstrating transient energy growths that disappear as $t \rightarrow \infty$.

References

- Blumsack, Steven L. and Gierasch, P. J. Mars: The effects of topography on baroclinic instability. *Journal of the Atmospheric Sciences*, 29(6):1081–1089, 1972. doi: 10.1175/1520-0469(1972)029<1081:MTEOTO>2.0.CO;2. URL [https://doi.org/10.1175/1520-0469\(1972\)029<1081:MTEOTO>2.0.CO;2](https://doi.org/10.1175/1520-0469(1972)029<1081:MTEOTO>2.0.CO;2).
- Vallis, Geoffrey K. *Atmospheric and Oceanic Fluid Dynamics: Fundamentals and Large-Scale Circulation*. Cambridge University Press, 2 edition, 2017. doi: 10.1017/9781107588417.